colloids and interfaces

MDPI

*Article*

# Solid Foams from Geopolymerization of Lunar Regolith Simulants Slurries

**Michela Elena Pedretti [1,2], Libero Liggieri [1,*], Luca Valentini [3], Giovanna Canu [1], Alberto Lagazzo [2], Francesca Ravera [1] and Eva Santini [1]**

[1] National Research Council, Institute of Condensed Matter Chemistry and Technologies for Energy (CNR-ICMATE), Unit of Genova, 16149 Genoa, Italy; michelaelenapedretti@cnr.it (M.E.P.); giovanna.canu@cnr.it (G.C.); francesca.ravera@cnr.it (F.R.); eva.santini@cnr.it (E.S.)
[2] Department of Civil, Chemical and Environmental Engineering, University of Genoa, 16145 Genoa, Italy; alberto.lagazzo@unige.it
[3] Department of Geosciences, University of Padua, 35131 Padua, Italy; luca.valentini@unipd.it
* Correspondence: libero.liggieri@cnr.it

**Abstract**

Robust, lightweight, and thermally insulating building materials, developed according to the In Situ Resource Utilization (ISRU) paradigm, are essential for enabling Moon settlements. With this aim, we have investigated the formulation and characterization of porous geopolymeric materials based on a lunar regolith simulant, focusing on the influence of surfactants and rheology-modifying additives on pore structure and final material performance. As an optimized procedure, a pre-formed TTAB foam was, in fact, incorporated into the geopolymeric precursor slurries to achieve a suitable porosity. Then, the effects of three thickeners (xanthan gum, bentonite, and Actigel-208) were evaluated in view of the possible utilization for the production of building blocks by 3D printing. Observations of the pore structure after the geopolymeric consolidation of the slurries showed predominantly closed-cell networks across all formulations, with a pore morphology strongly dependent on the thickener used. Xanthan gum promoted high porosity but reduced mechanical integrity, whereas bentonite produced denser structures with higher thermal conductivity. Actigel-208 provided the most balanced performance, combining adequate porosity with improved strength. These findings demonstrate the potential of producing thermally insulating, structurally stable solid foams from lunar regolith simulants via a geopolymerization route.

**Keywords:** porous materials; regolith; geopolymer; surfactants; thickener



Academic Editor: Spencer E. Taylor

Received: 10 March 2026
Revised: 10 April 2026
Accepted: 14 April 2026
Published: 16 April 2026



## 1. Introduction

The development of innovative materials for space infrastructure represents a complex challenge, as these materials must operate under extreme extraterrestrial conditions. These include low gravity, large temperature fluctuations, high vacuum, and exposure to micrometeoroid impacts [1,2]. The construction of habitable outposts on the Moon is widely recognized as a crucial intermediate step in the broader advancement of space exploration [3].

In this context, the ability to produce structural materials directly on the lunar surface is essential to reduce logistical costs and increase mission sustainability.

A key requirement for lunar construction is the adoption of In Situ Resource Utilization (ISRU) strategies, which aim to minimize dependence on raw material transport

from Earth by exploiting locally available resources such as lunar regolith [4–7]. Lunar regolith is a fine-grained, silica-rich particulate material that covers the Moon's surface. Its mineralogical composition and granulometry make it a promising feedstock for the synthesis of geopolymeric binders, which can be activated by alkaline solutions to form solid matrices suitable for construction [8–11].

Geopolymers have attracted considerable attention as alternative construction materials due to their high compressive strength, low permeability, good chemical durability, and excellent fire resistance [12–17]. Several studies have shown that geopolymer-based concretes can replace conventional Portland cement systems, often exhibiting superior mechanical performance and durability, while also offering reduced environmental impact through lower $CO_2$ emissions associated with their production [18,19].

Within the context of extraterrestrial construction, regolith-based geopolymers are particularly attractive because they enable the direct application of ISRU concepts, also by minimizing the water consumption, which for a large amount is released at the end of the consolidation process, and that can therefore be recovered [20]. Additional benefits of these materials are the potential for radiation shielding and for the mitigation of extreme thermal fluctuations on the lunar surface. To support their development, the use of regolith simulants allows researchers to replicate the mineralogical and granulometric characteristics of real lunar soil. These simulants provide a valuable platform for testing geopolymer formulations and foaming strategies under controlled laboratory conditions [21–24].

Among the possible fabrication methods, additive manufacturing (AM) through 3D printing has emerged as a particularly promising strategy, allowing the layer-by-layer construction of structural units directly from geopolymeric slurries [25,26].

One of the most promising directions in the development of regolith-based materials is the creation of porous geopolymeric structures with controlled morphology. These materials offer a combination of lightweight characteristics, thermal insulation, and adequate mechanical strength. Similar porous materials are widely used across terrestrial construction sectors and are produced through well-established technologies [27,28]. In recent years, these approaches have been increasingly adapted to geopolymeric systems, with several studies investigating the relationship between porosity, pore morphology, and mechanical and thermal performance [29–31].

The production of porous geopolymers typically relies on the generation of foamed slurries, which consolidate in porous networks with closed or open cells. Three primary approaches can be found in the literature to create porosity in geopolymeric systems: mechanical foaming, where a pre-formed foam is mixed with the slurry [32]; chemical foaming, which involves adding gas-releasing agents such as aluminum powder or hydrogen peroxide [33,34]; and physical foaming via gas injection, such as air or $CO_2$ insufflation during mixing [35]. Each method requires specific adjustments due to the unique rheological and chemical behavior of geopolymeric slurries. In particular, the interaction between the slurry's solid phase and the foaming agents plays a critical role in determining the final pore structure and stability, as well as the ability of the material to retain its shape after extrusion during 3D printing [36].

For the AM application, controlling the geopolymeric slurry rheology is particularly critical. The slurry must exhibit sufficient viscosity to maintain its shape during extrusion and prevent collapse of the printed layers, while remaining flowable enough to allow consistent deposition [26]. Therefore, thickening agents and viscosity modifiers are commonly employed to tailor the flow behavior of geopolymeric slurries without compromising foam stability or final mechanical performance of the porous geopolymer [37–39].

Different thickening agents are in fact tested in the present study, to identify the slurry composition that ensures proper rheological behavior for AM.

The foam morphology, including pore size distribution, connectivity, and uniformity, is further affected by the mixing conditions. The optimization of these parameters is crucial for achieving the desired balance between foam stability, structural integrity, and thermal insulation performance.

Therefore, the ultimate goal is to develop optimized processes and formulations for porous, regolith-based geopolymeric materials suitable for 3D printing and intended for use as construction elements in extraterrestrial habitats.

## 2. Materials and Methods

### *2.1. Raw Materials*

The geopolymeric materials are obtained by the reaction of the regolith simulant powder with an alkaline solution and the addition of a surfactant liquid foam, able to confer the final porous structure, and a thickening agent, which modifies the rheological behavior of the slurry.

#### 2.1.1. Regolith Simulant and Solid Geopolymeric Precursors

The simulant and primary solid precursor employed in this study was the lunar regolith simulant LMS-1D (Lunar Mare Simulant 1 Dust) produced by Space Resource Technology (Oviedo, FL, USA). This product simulates the fine granulometry of the lunar mare dust, with about 80% of the particles having sizes below 10 μm and nearly 100% below 30 μm. This simulant is composed for the largest part, 75%, by aluminosilicates. More details about its production, composition, and features are available in refs. [40].

The use of a regolith-based aluminosilicate source enables the adaptation of established geopolymer processing strategies to materials representative of ISRU-oriented construction systems.

Metakaolin (MK, Imerys MetaStar 501, Imerys, Paris, France) was used as an additional reactive aluminosilicate component to promote geopolymerization and improve matrix homogeneity. The addition of metakaolin was also intended to better approximate the amorphous aluminosilicate content of actual lunar regolith, which is higher compared to that present in LMS-1D [22], consequently enhancing the material reactivity.

#### 2.1.2. Alkaline Activating Solution

The aluminosilicate powders (LMS-1D and metakaolin) were activated using an alkaline solution to produce alkali-activated binders. The activating solution was prepared by dissolving sodium hydroxide (NaOH, 99% purity, Riedel-de-Haën, Hannover, Germany) pellets in ultrapure water (Milli-Q, Millipore, Burlington, MA, USA), followed by the addition of sodium silicate solution (Honeywell, Morris Plains, NJ, USA) under stirring until complete homogenization. The solution was allowed to equilibrate for at least 3 h prior to mixing with the solid precursors.

#### 2.1.3. Surfactant

The cationic surfactant tetradecyltrimethylammonium bromide (TTAB, Sigma-Aldrich/Merck, Darmstadt, Germany) was selected as a foaming agent due to its effective interfacial activity and foam stabilization capability [41,42] together with its relatively low cost, making it attractive for potential scale-up and industrial applications. TTAB presents a Critical Micelle Concentration (CMC) in water of $4 \times 10^{-3}$ M. Cationic surfactants in negative particle dispersions are also able to create amphiphilic complexes by adsorbing on these particles, which in turn may contribute to increasing the stability of the obtained foams.

2.1.4. Thickening Agents

To regulate rheology and structural build-up of the fresh slurry, three thickening agents were investigated:

- Xanthan Gum (XG, Erbotech, Esine, Italy): used as a 0.1 wt.% aqueous solution. XG is a polysaccharide characterized by strong shear-thinning behavior and the ability to increase yield stress [43,44].
- Na-bentonite (ClearOFF Minerals, Ashreigney, UK): a high-purity montmorillonite clay. Its swelling capacity and morphology increase viscosity and improve structural build-up [45].
- ActiGel-208 (Active Minerals, Sparks, MD, USA): a magnesium aluminosilicate nanofiber additive commercialized as a strong thixotropic agent. Its fibrillar structure promotes network formation within the slurry, improving both thixotropy and resistance to collapse [46].

Thickeners were incorporated to balance viscosity and shape retention, necessary for 3D printing applications, while maintaining sufficient fluidity for air incorporation.

### *2.2. Optimization of Alkali-Activated Binder Composition*

An optimal formulation for the alkali-activated binder was selected based on previous experiments relying on a Design-of-Experiments (DoE) approach, which envisaged the variation in the solution $SiO_2/Na_2O$ molar ratio (0.8 to 1.6), solution/powder ratio (0.4 to 0.44), and metakaolin addition (0 to 15 wt.%). Details of the procedure are reported elsewhere [47]. The final formulation, named Opt2, as mentioned in the ref. [47], was selected as a trade-off between the strength and amount of added MK, with the aim of minimizing the latter. Specifically, it comprised 8.5 wt.% MK added to the LMS-1D simulant, a $SiO_2/Na_2O$ molar ratio of 1.5 for the sodium silicate solution, and a solution/powder ratio of 0.41.

### *2.3. Development of Foamed Geopolymer Formulations*

Foamed geopolymeric slurries were developed starting from the reference alkali-activated binder formulation Opt2 described in Section 2.2. This formulation was progressively modified through the addition of specific additives, aimed at ensuring adequate rheological behavior and foam stability.

Four Opt2-based foamed systems were prepared: a reference formulation containing only TTAB and three additional formulations obtained by incorporating one of the selected thickening agents. The compositions of the investigated Opt2-based foamed formulations, expressed per 100 g of total mixture, are summarized in Table 1.

**Table 1.** Composition of investigated foamed formulations.

| Foamed Formulation | LMS-1D (wt.%) | MK (wt.%) | Alkaline Solution (wt.%) | TTAB $4 \times 10^{-2}$ M (wt.%) | Thickener | Thickener (wt.%) |
|---|---|---|---|---|---|---|
| **1** | 64.89 | 6.03 | 20.51 | 8.56 | - | - |
| **2** | 64.19 | 5.91 | 24.22 | 2.83 | XG (0.1%) | 2.83 |
| **3** | 61.86 | 5.75 | 25.64 | 3.38 | Bentonite | 3.38 |
| **4** | 64.52 | 5.99 | 26.19 | 1.75 | Actigel-208 | 1.5 |

### *2.4. Foam Generation and Mixing Procedure*

#### 2.4.1. Foam Formulation

Based on preliminary exploratory tests, the incorporation of a pre-formed aqueous foam into the geopolymer slurry resulted in the most promising approach to obtain stable, air-entrained slurries, suitable for being consolidated into porous materials.

The stability of foams obtained from TTAB aqueous solutions of various concentrations was then investigated. The foams were obtained using a homogenizer (Ultraturrax T25 Digital, IKA-Werke, Staufen, Germany) at 10,000 rpm for 3 min.

Figure 1 reports the relative height of the studied foams as a function of the aging time. The studied concentrations span from 0.1 × CMC to 10 × CMC.

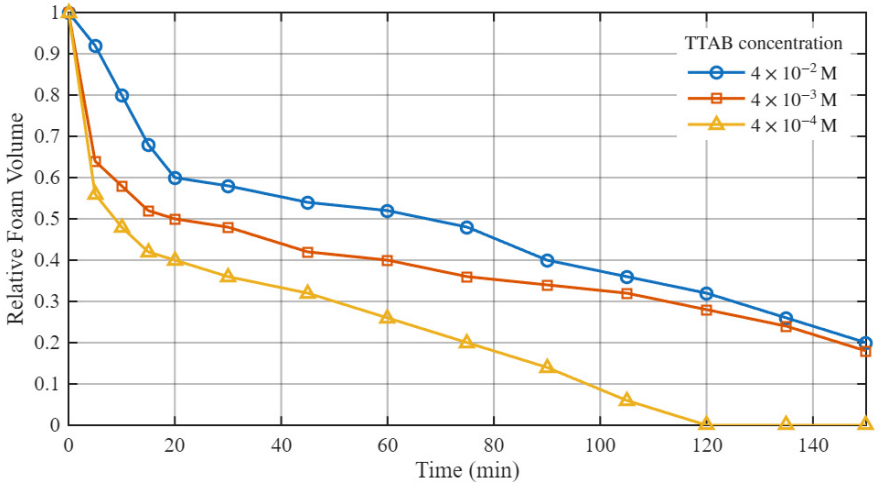


**Figure 1.** Aging of foams obtained from bare TTAB aqueous solutions. See the text for details.

Considering the operative and processing time constraints set by the protocol for obtaining the final materials (see next section), we followed the straightforward approach of incorporating the most stable foam, obtained with a TTAB concentration of $4 \times 10^{-2}$ M (10 × CMC). As for the above figure, after an initial stage of relatively quick destabilization, this foam enters a different regime, exhibiting about one hour of slow destabilization: sufficient for the purpose of incorporating it into the slurry.

#### 2.4.2. Foamed Geopolymer Production Protocol

Based on preliminary trials, an optimized procedure was developed.

All the reagents involved in the materials production were mixed together by mechanical stirring using a two-bladed shaft connected to a motor (RW16 basic, IKA-Werke, Staufen, Germany) while the pre-formed TTAB foam was obtained separately, as described above.

In more detail, the preparation of the foamed geopolymer slurry was carried out according to the following protocol:

1. The alkaline activating solution was stirred at low speed using a two-bladed shaft.
2. The powder mixture (LMS-1D and MK) was gradually added to the activating solution and mixed for 15 min to ensure homogeneity.
3. The selected thickening agent, when included, was incorporated, and mixing continued for an additional 15 min to achieve the desired rheological properties.
4. In parallel, the TTAB-based liquid foam was prepared.
5. The pre-formed foam was added to the geopolymeric slurry, and the mixture was carefully blended using a spatula to ensure uniform bubble distribution while minimizing bubble rupture and foam collapse, then poured into a container (plastic or silicone) of the desired shape.

6. These samples were left at room temperature for 48 h, during which they hardened under the effect of the spontaneous geopolymerization process. However, to ensure complete moisture removal and full stabilization of the material, characterization was performed after at least two weeks of curing under room conditions.

### 2.5. Interfacial Characterization of the Dispersion

An alternative possibility for obtaining aired slurries is represented by the direct incorporation of the TTAB solution into the dispersions to be foamed. In principle, this approach warrants the possibility of decreasing the quantity of surfactant. It is in fact well known [48,49] that under specific conditions, particles may interact even with small amounts of surfactants, forming amphiphilic complexes which, segregating at the interface and changing its mechanical properties (surface tension and rheology), act as efficient foam stabilizers. The occurrence of these interactions, if any, can be effectively studied and characterized based on the interfacial properties of these mixed particle-surfactant dispersions.

To this aim, measurements of the dynamic surface tension (ST) at 20 °C were performed at the air-dispersion interface using a Pendant Drop Tensiometer (PAT-1, Sinterface, Berlin, Germany). The tensiometer warrants an accuracy of ±0.1 mN/m on the measurement of the ST of a drop formed at the tip of a stainless steel capillary, whose area is kept constant during the duration of the test. According to a standardized procedure, the drop to be measured is quickly formed at the tip of the capillary, in order to create a "fresh" surface, that is, nearly free from surfactant. The ST of the drop is then monitored as the process of adsorption of the surface-active species progresses.

LMS-1D particles exhibit a bimodal size distribution, comprising a submicron fraction (<1 μm) and a second fraction centered around approximately 10 μm. The larger particle fraction tends to settle rapidly right after the dispersion preparation. That makes the use of the whole dispersion unsuitable for ST measurements, since the particle settlement creates non-homogeneous conditions in the sample. On the other hand, it is reasonable to consider that the interfacial properties of the dispersion, being determined by microscopic effects, are related to the particle submicron fraction. The latter, being less prone to spontaneous segregation, remains in the supernatant and can be suitably utilized for tensiometric measurements. Thus, only with the purpose of investigating the interfacial properties, a suspension of 30 wt.% of LMS-1D in water was prepared. After waiting 16 h for the deposition of bigger particles, the supernatant was removed. Dynamic Light Scattering (Zetasizer, Malvern Panalytical, Malvern, UK) measurements of the particle size in the supernatant provide an average value for the particle diameter of 560 nm with a standard deviation of 71 nm. By weighing known volumes of supernatant and of their dry residuals, it was possible to estimate a particle concentration of the supernatant of the order of 0.01 wt.%.

To prepare the supernatant dispersions containing the surfactant, a proper volume of TTAB solution was added dropwise and under stirring to a proper volume of supernatant dispersion, in order to obtain, in the whole dispersion volume, uniform concentration conditions for possible interactions between the surfactant molecules and the particles.

### 2.6. Physical and Mechanical Characterization

#### 2.6.1. Microscopic Analysis

After consolidation, the samples were examined using a Scanning Electron Microscope (SEM, LEO 1450VP, LEO Electron Microscopy Ltd., Cambridge, UK), and a Leica DVM6 optical microscope (Leica Microsystems GmbH, Hamburg, Germany), to assess pore morphology and distribution. The size distribution was obtained from the optical

microscopy images using the tools of the above optical microscope proprietary software (Leica Application Suite X-v3.0.4, Leica Microsystems GmbH, Hamburg, Germany).

#### 2.6.2. Density and Porosity

Cylindrical specimens were prepared for density and porosity determination. Geometric density was calculated as the ratio between specimen mass and measured volume.

The relative density, $\varrho_{rel}$, was calculated as the ratio between the sample density and its theoretical density. The density of the geopolymeric material, including the added components, was obtained by grinding consolidated samples and measuring their true density using a helium pycnometer (AccuPyc 1330, Micrometritics, Norcross, GA, USA). Porosity was then calculated as $(1 - \varrho_{rel})$.

#### 2.6.3. Thermal Conductivity

Thermal conductivity was measured using an optical thermal conductivity scanner (TCSCAN, Schwab Research Technology, Achim, Germany). Prior to testing, one face of each sample was coated with a thin layer of black acrylic paint to minimize reflection effects. The calibration standards used for thermal conductivity measurements ranged from 0.71 to 1.35 $W \cdot m^{-1} \cdot K^{-1}$ and they were selected as being those with values closer to the expected conductivity range, based on published data on foamed alkali-activated materials [50,51].

#### 2.6.4. Compressive Strength and Elastic Moduli

Mechanical performance was evaluated through uniaxial compressive strength tests conducted on cubic specimens ($25 \times 25 \times 25$ $mm^3$) using a testing machine (ZwickRoell Z05, Zwick-Roell, Ulm, Germany) equipped with a load cell of 50 kN. The stress–strain response was recorded to determine compressive strength and elastic moduli for the investigated systems.

## 3. Results

### *3.1. Interfacial Characterization of the Supernatant Dispersion in the Presence of TTAB*

As detailed in Section 2.5, the possible interaction effects between the TTAB and the submicrometric fraction of the simulant particles in the supernatant were investigated by surface tension measurements. In particular, the ST of TTAB solutions was compared with that of the supernatant of the original LMS-1D dispersion, loaded with corresponding quantities of TTAB. The dynamic ST of these dispersions for increasing quantities of TTAB is reported in Figure 1. In the absence of TTAB (TTAB concentration = 0 M), the bare particles are essentially not surface active, since the corresponding dynamic ST shows values similar to those of pure water and practically no decrease. Dispersions formulated with the addition of a small amount of TTAB, up to $2 \times 10^{-5}$ M, show a similar behavior. Increasing further the concentration of TTAB, all systems exhibit a progressive decrease in ST over time, approaching a plateau after about 1 h, which we can conventionally assume as a near-equilibrium ST. As shown in Figure 2, a clear trend is observed for these near-equilibrium values: increasing the TTAB concentration leads to a progressive reduction in it, as for a common surfactant. For concentrations higher than $3 \times 10^{-3}$ M, the near-equilibrium ST shows a practically constant value around 36 mN/m, similar to the CMC behavior in a common surfactant.

When comparing these results with those of the corresponding bare TTAB solutions, the latter show systematically larger values of the equilibrium ST, as also shown in Figure 3. Both curves, however, achieve the same ST above the CMC, which, however, appears at slightly lower concentration for the simulant dispersion.

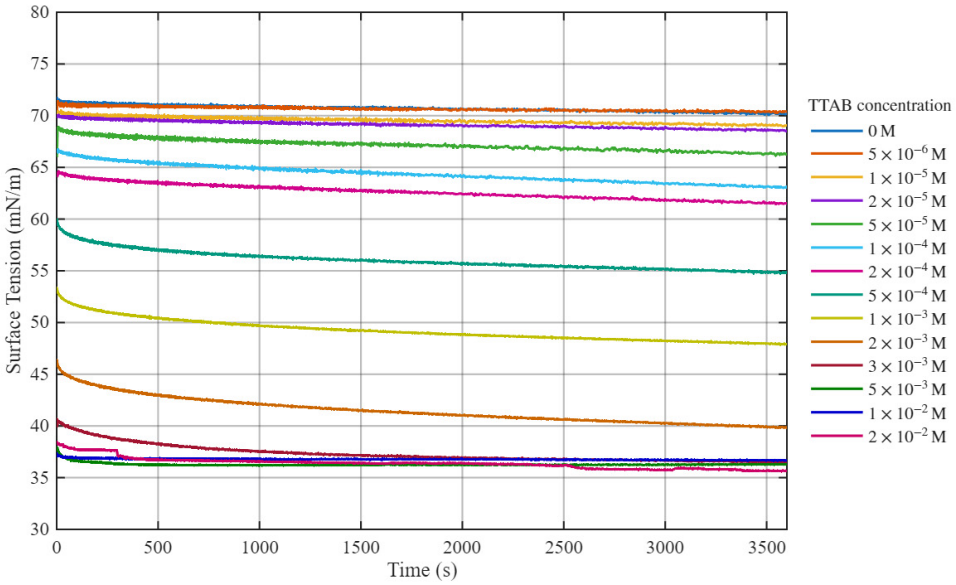


**Figure 2.** Time evolution of surface tension for the supernatant of LMS-1D 30 wt% dispersion versus the added TTAB concentration. See text for details.

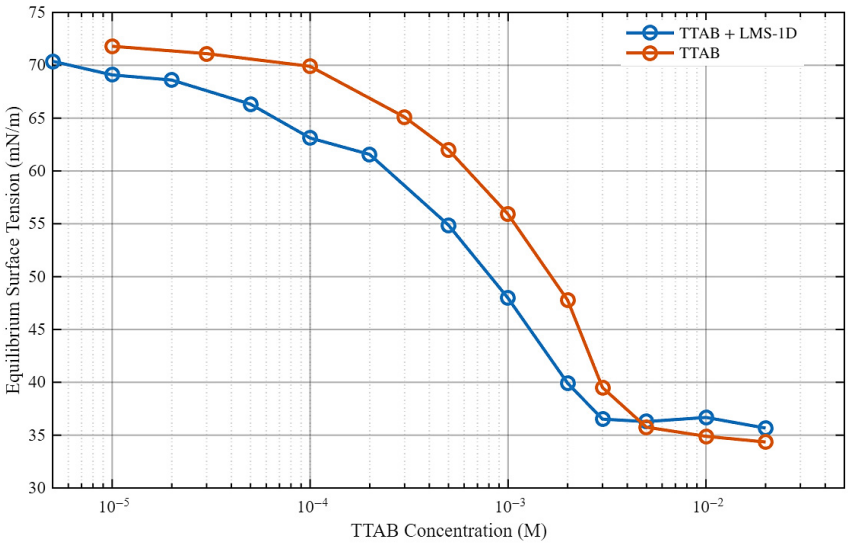


**Figure 3.** Comparison between the measured equilibrium ST of the supernatant of the 30% simulant dispersion additivated by TTAB (see text for details) and that of the corresponding TTAB aqueous solution (latter data taken from Lamch et al. [52]).

The typical signature that one would expect from the interaction between TTAB and particles are larger values of ST in the region up to about 0.1 × CMC. This is, in fact, the most evident effect of the depletion of the free surfactant molecules, caused by the adsorption of the surfactant at the particle surface. The behavior observed here is instead reminiscent of that commonly reported for cationic surfactant solutions in the presence of small ionic salt quantities: see, for example, the results for similar alkyltrimethylammoniumbromides in the presence of small quantities of monovalent salts, as reported in the supplementary material of ref. [52], or of NaCl in ref. [53]. In fact, for these systems, the adsorption of the surfactant at the aqueous surface is favored, while its CMC decreases due to the decreased surfactant solubility in the salty solution. On that basis, it is therefore reasonable to speculate that the differences observed for the ST of the supernatant dispersion of simulant in the presence of TTAB are due to ionic salt impurities that may be present in the powders. The measured value of the conductivity of the supernatant in the absence of

TTAB is 233 μS/cm, corroborating this hypothesis. At present, we do not have evidences to speculate about the nature of the ionic species. However, just as an example, for NaCl, this conductivity corresponds to a concentration close to about 2 mM. For this order of NaCl concentration in CTAB solutions, reductions in the ST of the order of 5–10 mN/m are reported, which are fully compatible with what is observed here. According to these results, for the studied mixed dispersions obtained with the supernatant, there is little evidence of the presence of amphiphilic particle-surfactant complexes useful to enhance the stability of a foam. Therefore, at least under the described conditions, there are no advantages in using the supernatant to formulate the pre-formed foam to be incorporated in the slurry.

### *3.2. Solid Materials Characterization*

The hardened samples resulting from the geopolymerization process were analyzed to evaluate the influence of surfactant concentration, mixing method, and thickening agents on the final microstructure and functional properties. All samples were prepared using the pre-formed TTAB foam incorporation procedure, according to the optimized protocol summarized in the above Section 2.4.2.

#### 3.2.1. Microscopic Analysis

In the consolidated sample containing only TTAB (blank formulation) and no other additives, optical microscopy observations revealed a porous structure characterized by a relatively uniform pore distribution, consisting of small, mostly spherical pores and occasional larger voids. Most pores exhibited diameters in the 100–200 μm range, and the structure appeared to comprise predominantly closed cells (Figure 4a). To further investigate pore morphology at higher magnification, SEM analysis was employed, revealing the presence of additional smaller pores with diameters down to approximately 35 μm, while confirming that the porosity was mainly closed, with no clear evidence of interconnected macroporous channels (Figure 4b).

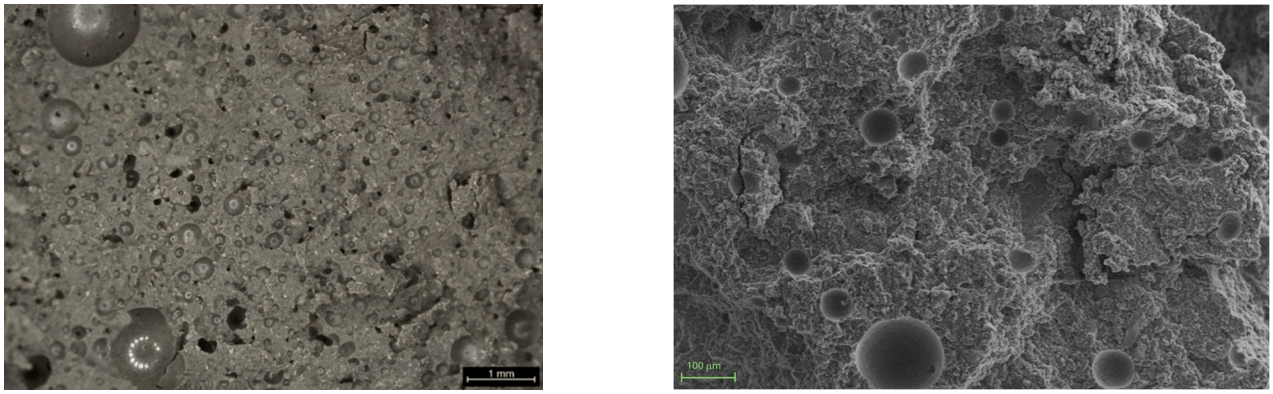


(**a**) (**b**)

**Figure 4.** Microscopic images of the foamed geopolymer formulated with the sole TTAB (no thickeners), obtained with: (**a**) optical microscope; (**b**) SEM.

The sample containing 0.1 wt% XG solution exhibited a high density of large pores (Figure 5a), mostly within the 200–400 μm range. Smaller pores, with diameters around 70 μm, were frequently observed within these larger voids. The structure appeared heterogeneous, with thin pore walls and regions of local structural discontinuity. In contrast, bentonite-containing samples exhibited lower apparent porosity and a more compact structure. The overall morphology appeared denser, with thicker solid walls separating the pores (Figure 5b). The pores were less spherical and displayed higher polydispersity, with the presence of larger, elongated pores and smaller, more regular ones. In both types of

samples, most pores were found within the 100–150 µm range. Actigel-208 demonstrated intermediate behavior (Figure 5c) among the tested thickeners. The pore distribution was more homogeneous than in the bentonite system, with most pores again falling within the diameter range of 100–150 µm. The pore size distribution in the samples containing bentonite and Actigel-208 was quantitatively evaluated based on the analysis of several optical images, taken randomly along each sample. These distributions are plotted in Figure 6, and the corresponding average diameters and widths are given in Table 2, confirming that for both types of utilized thickeners the resulting pore diameters lie mostly within the 100–150 µm range.

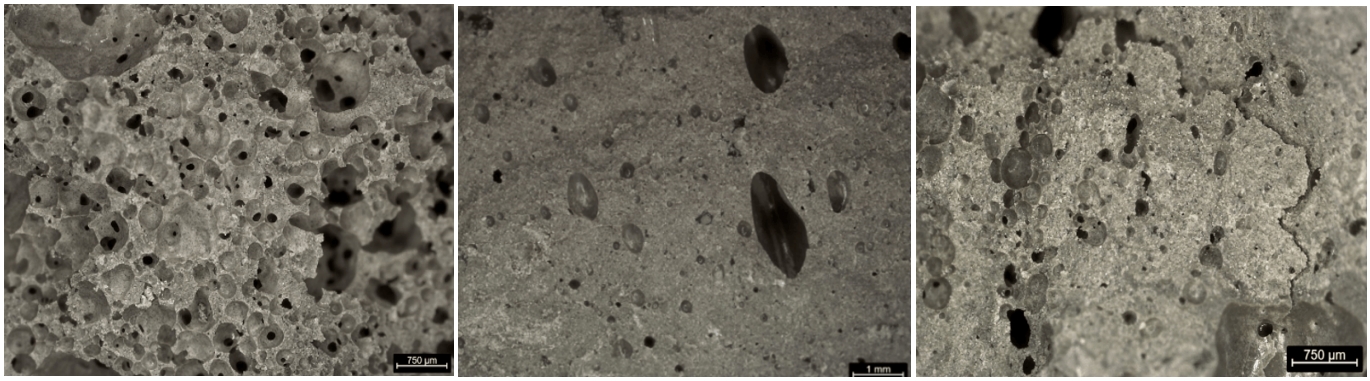


(**a**) (**b**) (**c**)

**Figure 5.** Optical images of foamed geopolymer samples containing different thickening agents, as for Table 1: (**a**) Xanthan gum (0.1 wt.%); (**b**) Bentonite; (**c**) Actigel-208.

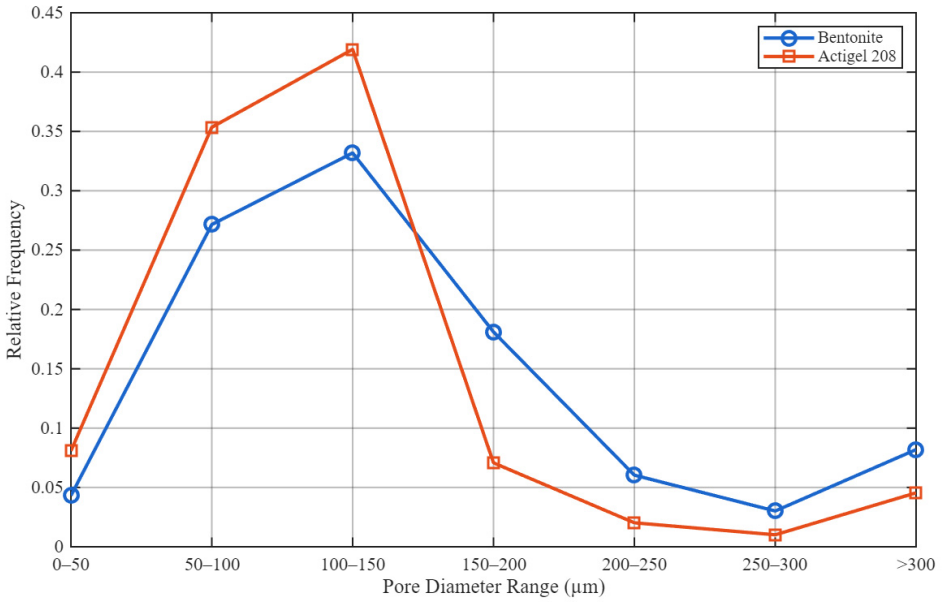


**Figure 6.** Relative number frequency of the pore size distribution from the analysis of optical images of foamed geopolymer samples containing 0.1 wt.% of Bentonite (circles) and Actigel-208 (squares).

**Table 2.** Average pore diameter of foamed geopolymer samples containing 0.1 wt.% of Bentonite and Actigel-208, calculated from the pore size distributions plotted in Figure 5.

| | **Bentonite** | **Actigel-208** |
|---|---|---|
| Average pore diameter (µm) ± SD | 149.4 ± 107.6 | 126.6 ± 86.3 |

It is important to underline that the size distribution analysis was carried out only for the samples obtained with Bentonite and Actigel-208, since they exhibit the most regular pore structure. For the samples containing XG, the presence of large irregular cavities prevented a reliable quantitative analysis, while the qualitative pore size ranges reported above remain valid.

#### 3.2.2. Porosity

Considering a solid matrix density of 2.8163 g/cm$^3$, measured by the pycnometer, the total porosity of the samples obtained with the different thickeners was calculated. The results are summarized in Table 3, reporting the values measured for two samples of the same type and their average value. Among the investigated formulations, the sample containing 0.1 wt.% XG solution exhibited the highest porosity, with a value comparable to that of the formulation prepared without additives (blank). In contrast, the addition of bentonite and Actigel-208 resulted in lower porosity values, indicating the formation of a denser structure. It is also useful to notice that the value reported in Table 3 for the relative percent difference between the values measured for the two samples formulated with the same thickener, briefly indicated as Δ-reflects the same gradation in the regularity of the pore structure emerging from the microscopy analysis, discussed in the previous section.

**Table 3.** Total porosity of foamed geopolymer samples. The table reports the values measured for two samples formulated with the same thickener, their average value, and the relative difference (Variance) between the two values.

| Porosity (%) | Blank | Xanthan Gum | Bentonite | Actigel-208 |
|---|---|---|---|---|
| Sample 1 | 51.9 | 55 | 38.9 | 35.3 |
| Sample 2 | 50.7 | 51.3 | 39.5 | 36.8 |
| Average | 51.3 | 53.1 | 39.2 | 36.1 |
| Δ (%) | 2 | 7 | 2 | 4 |

#### 3.2.3. Thermal Conductivity

Thermal conductivity measurements are summarized in Table 4. Compared to the sample containing only TTAB, the addition of bentonite and Actigel-208 resulted in a marked increase in thermal conductivity, reaching approximately twice the value of the blank sample. On the other hand, the incorporation of 0.1 wt.% XG solution resulted in a slight reduction in the insulating properties. The values reported in the Table are the average of five different samples formulated with the same thickener. The maximum and minimum measured values for each type show a variability of the order of ±10%, calling for a good homogeneity of this property over the material.

**Table 4.** Thermal conductivity values of foamed geopolymer samples prepared with different, or none, thickening agents. For each type, the reported value is the average of measurements performed on five different samples. The maximum and minimum values of these measurements are also reported.

| | Blank | Xanthan Gum | Bentonite | Actigel-208 |
|---|---|---|---|---|
| Thermal conductivity ($W \cdot m^{-1} \cdot K^{-1}$) | 0.348 | 0.300 | 0.695 | 0.719 |
| Range (min–max) | 0.296–0.381 | 0.269–0.327 | 0.647–0.761 | 0.660–0.769 |

#### 3.2.4. Compressive Strength and Elastic Moduli

Figure 7 shows examples of the compressive stress–strain curves of foamed geopolymer samples containing different thickening agents. A clear dependence of the mechanical

response on the type of thickener is observed. The sample containing bentonite exhibits the highest compressive strength, with a steep initial slope and a peak stress close to nine MPa before failure, indicating higher stiffness and a more resistant pore structure.

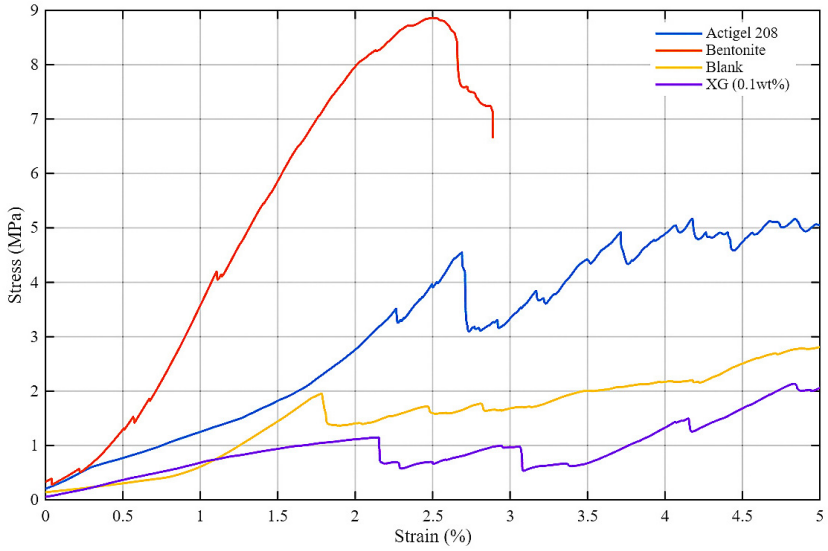


**Figure 7.** Examples of the compressive stress–strain curves of foamed geopolymer samples prepared with different thickening agents.

This behavior is confirmed by the elastic modulus (Ec), which reaches 442 MPa for the bentonite-based formulation, as reported in Table 5. The latter Table reports, in fact, the highest stiffness observed during the compression tests for two samples formulated with the same thickener. The samples formulated with Actigel-208 show an intermediate behavior, with a maximum stress around 5 MPa. The curve is characterized by local drops, suggesting progressive pore collapse and subsequent structural rearrangement within the porous matrix. Its elastic modulus (Ec = 234 MPa) reflects a moderately stiff but more deformable structure compared to the bentonite system. The sample containing no thickeners presents lower compressive strength, while the XG solution formulation displays the weakest mechanical performance, with limited stress development, instability during compression, and the lowest elastic modulus. It is useful to observe that the described behavior correlates with the regularity of the pore structure observed in the previous section for the materials formulated with the different thickeners, which is also reflected by the values of Δ reported in Table 5. Overall, the samples characterized by a more porous internal structure exhibit higher friability, as reflected in the non-linear behavior of the stress–strain curves. After the initial fracture, the curves display successive stress drops associated with progressive pore collapse and densification of the material during further compression.

**Table 5.** Elastic modulus (Ec) obtained from compressive stress–strain curves for the investigated foamed geopolymer formulations. The table reports the values measured for two samples formulated with the same thickener, their average value, and the relative difference (Variance) between the two values.

| Elastic Modulus (MPa) | Blank | Xanthan Gum | Bentonite | Actigel-208 |
|---|---|---|---|---|
| Sample 1 | 161.8 | 66.0 | 447.7 | 231.8 |
| Sample 2 | 173.5 | 58.8 | 436.8 | 237.3 |
| Average | 167.7 | 62.4 | 442.3 | 234.6 |
| Δ (%) | 7 | 12 | 2 | 2 |

The two panels of Figure 8 report the thermal conductivity and the compressive strength of all studied materials as a function of their density. As can be appreciated, the thermal conductivity shows a remarkable direct correlation with the density of the materials for all formulations. A similar correlation can also be appreciated for the compressive strength, for all materials, except the one formulated with Xanthan Gum. This is again a consequence of the observed heterogeneity of pore structure observed in the latter material that, even having the largest density, presents a large intrinsic fragility.

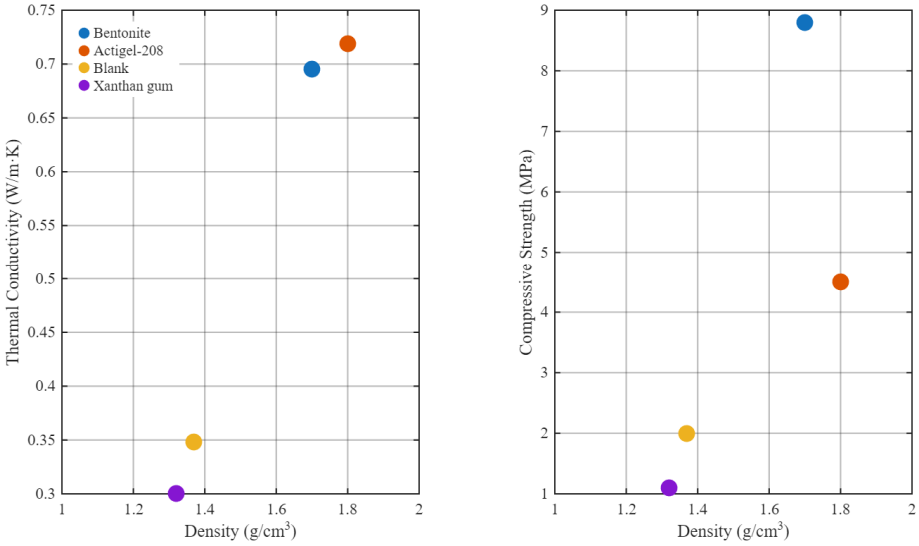


**Figure 8.** Thermal conductivity (**left**) and compressive strength (**right**) of the produced materials as a function of their densities.

## 4. Discussion

The extreme environmental conditions of the Moon, characterized by large thermal excursions, vacuum, and reduced gravity, require materials capable of combining thermal insulation and sufficient mechanical strength [1].

The results obtained in this work demonstrate that these requirements can be addressed through the careful design of surfactant-stabilized foams and the optimization of slurry rheology, via the selection of appropriate additives. Interfacial measurements revealed that the interaction with LMS-1D particles and the possible formation of amphiphilic complexes [54,55] play a secondary role with respect to potential ionic impurities that may be present in the dispersion. Such a conclusion holds, however, for the large TTAB concentrations utilized here for the formulation of the pre-formed foam. However, with the aim of increasing the ISRU interest of this research, a consistent reduction in the amount of surfactant to be transported from Earth is a valuable objective. In that case, the mentioned interaction, between the cationic surfactant and the predominantly negatively charged particles of the regolith components, could become a key factor for the formation and stabilization of the foam instead, as already assessed by several works [56–59]. That will therefore be one important research direction for the next investigations on the subject.

Microscopic observations showed that the consolidated materials exhibit predominantly closed-cell porosity. This feature is particularly relevant for lunar applications, as closed pores reduce convective heat transfer and enhance thermal insulation while preserving structural continuity of the matrix. The stability of the initial liquid foam was found to directly influence the final pore architecture, highlighting the strong link between fresh-state interfacial phenomena and hardened-state performance.

The addition of thickening agents played a crucial role in modulating foam retention and final material properties. XG solution allowed the incorporation of a larger volume of

foam, resulting in the highest total porosity, lowest thermal conductivity, and enhanced insulation performance. However, this highly porous structure exhibited the lowest compressive resistance, reflecting the trade-off between porosity and mechanical stiffness in cellular materials [60–62].

Bentonite and Actigel-208 significantly increased slurry viscosity, limiting bubble expansion and leading to lower porosity values. This densification resulted in higher thermal conductivity, due to the reduced air content and the thicker solid walls separating the pores. At the same time, mechanical performance improved markedly. The bentonite-based formulation exhibited the highest elastic modulus and compressive strength, indicating a more efficient load-bearing structure, whereas Actigel-208 showed intermediate mechanical features, suggesting a pore architecture that, although similar in overall porosity to bentonite, may differ in terms of wall thickness distribution or structural homogeneity.

These observations highlight how the material's structure directly governs its performance. Increased porosity enhances thermal insulation but reduces stiffness and strength, whereas reduced porosity improves mechanical resistance at the expense of insulation performance. The correlation observed between porosity, thermal conductivity, and elastic modulus is consistent with the mechanical behavior of cellular solids, where elastic modulus scales with relative density [60,62]. The rheological control exerted by the thickening agents, therefore, directly determines pore architecture and, consequently, the macroscopic thermal and mechanical response.

Among the tested formulations, both Actigel-208 and bentonite appear attractive candidates when considering the combined requirements of thermal insulation and mechanical performance. They provide the most balanced compromise between porosity, insulation capability, and structural integrity, making them particularly suitable for AM of lightweight regolith-based components.

Overall, these findings confirm that surfactant-stabilized foamed geopolymers based on lunar regolith simulants provide a viable route for producing lightweight, thermally insulating construction elements. By tailoring interfacial properties and slurry rheology, it is possible to optimize the balance between insulation and mechanical performance, paving the way for AM of structural components in future lunar habitats.

Although these results are promising, several limitations must be acknowledged. All experiments were conducted under terrestrial and laboratory room conditions, while the influence of reduced gravity, reduced atmosphere, and lunar dust electrostatics on foam formation and consolidation remains to be investigated. Moreover, from an ISRU perspective, water recovery during the geopolymerization process needs to be studied to ensure efficient use of this precious resource in a lunar environment. Accordingly, studies are underway to explore geopolymer formulations that reduce water demand, replacing liquid foams with porogenous agents, aiming at simplifying and validating the foaming process under realistic lunar conditions and to enhance even more its suitability for 3D printing.

Additionally, alternative surfactants and stabilizers even more compatible with ISRU constraints will be evaluated. A particularly interesting route in that direction could be the exploitation of the enhanced foam stabilization properties that may emerge from the associations of surfactants with the submicrometric fraction of regoliths, after developing more efficient procedures to extract and concentrate it. In fact, even if the study of the interfacial properties presented here did not provide positive evidence, that could be the result of the small load of solid particles in the supernatant. The possibility of working with more concentrated dispersions of submicrometric regolith could open new interesting routes for investigating these synergetic effects with surfactants.

**Author Contributions:** Conceptualization, L.L. and E.S.; Data curation, M.E.P., L.V., G.C., A.L. and E.S.; Formal analysis, L.L., F.R. and E.S.; Funding acquisition, L.V., E.S. and F.R.; Investigation, M.E.P., L.V. and E.S.; Methodology, M.E.P. and E.S.; Supervision, E.S.; Writing—original draft, M.E.P. and L.L.; Writing—review and editing, L.L., F.R. and E.S. All authors have read and agreed to the published version of the manuscript.

**Funding:** This research was funded and supervised by the Italian Space Agency (Agenzia Spaziale Italiana, ASI) in the framework of the project "Geopolymers for Lunar Additive Manufacturing and Sensing-GLAMS", contract no. ASI-2023-6-U. Part of the activities were also funded by the Italian Space Agency (ASI) and the Italian Ministry of University and Research (MUR), under the project SPACE IT UP!–Spoke 8: "Robotic and Human Exploration of Extraterrestrial Habitats, Architectures and Infrastructures", contract no. ASI-2024-5-E.0.

**Data Availability Statement:** The raw data supporting the conclusions of this article will be made available on request.

**Acknowledgments:** The authors wish to thank Claudia Esposito, GLAMS for the Italian Space Agency, for her proactive support in the successful implementation of the project. The authors used ChatGPT 5.3 for the purposes of generating images that have been assembled in the Graphical Abstract. The authors have reviewed and edited the output and take full responsibility for the content of this publication.

**Conflicts of Interest:** This manuscript was submitted with the approval of the funder, Italian Space Agency (ASI). The authors declare no conflicts of interest.

## Abbreviations

The following abbreviations are used in this manuscript:

| | |
|---|---|
| ISRU | In Situ Resource Utilization |
| AM | Additive Manufacturing |
| LMS-1D | Lunar Mare Simulant 1 Dust |
| MK | Metakaolin |
| TTAB | Tetradecyltrimethylammonium bromide |
| CMC | Critical Micelle Concentration |
| ST | Surface Tension |
| XG | Xanthan Gum |
| SEM | Scanning Electron Microscopy |

## References

1. Vaniman, D.; Reedy, R.; Heiken, G.; Olhoeft, G.; Mendell, W. The Lunar Environment. In *Lunar Sourcebook*; Cambridge University Press: Cambridge, UK, 1991; Volume 1, pp. 27–60.
2. Bayar, B. Designing Extraterrestrial Habitats on Mars and the Moon: An Overview of Environmental Conditions and Design Considerations. In *Proceedings of the 4th International Civil Engineering and Architecture Conference*; Springer: Singapore, 2025; pp. 211–221.
3. Casini, A.E.M.; Maggiore, P.; Viola, N.; Basso, V.; Ferrino, M.; Hoffman, J.A.; Cowley, A. Analysis of a Moon Outpost for Mars Enabling Technologies through a Virtual Reality Environment. *Acta Astronaut.* **2018**, *143*, 353–361. [CrossRef]
4. Anand, M.; Crawford, I.A.; Balat-Pichelin, M.; Abanades, S.; van Westrenen, W.; Péraudeau, G.; Jaumann, R.; Seboldt, W. A Brief Review of Chemical and Mineralogical Resources on the Moon and Likely Initial in Situ Resource Utilization (ISRU) Applications. *Planet. Space Sci.* **2012**, *74*, 42–48. [CrossRef]
5. Zhang, P.; Dai, W.; Niu, R.; Zhang, G.; Liu, G.; Liu, X.; Bo, Z.; Wang, Z.; Zheng, H.; Liu, C.; et al. Overview of the Lunar In Situ Resource Utilization Techniques for Future Lunar Missions. *Space Sci. Technol.* **2023**, *3*, 0037. [CrossRef]
6. Wang, C.; Zhang, G.; Wang, Y.; Song, L. A Review of Lunar Environment and In-Situ Resource Utilization for Achieving Long-Term Lunar Habitation. *Galaxies* **2025**, *13*, 103. [CrossRef]
7. Valentini, L.; Moore, K.R.; Bediako, M. Sustainable Sourcing of Raw Materials for Construction: From the Earth to the Moon and Beyond. *Elements* **2022**, *18*, 327–332. [CrossRef]

8. Zhang, R.; Zhou, S.; Li, F. Preparation of Geopolymer Based on Lunar Regolith Simulant at In-Situ Lunar Temperature and Its Durability under Lunar High and Cryogenic Temperature. *Constr. Build. Mater.* **2022**, *318*, 126033. [CrossRef]
9. Xiong, G.; Guo, X.; Yuan, S.; Xia, M.; Wang, Z. The Mechanical and Structural Properties of Lunar Regolith Simulant Based Geopolymer under Extreme Temperature Environment on the Moon through Experimental and Simulation Methods. *Constr. Build. Mater.* **2022**, *325*, 126679. [CrossRef]
10. Zheng, X.; Zhao, C.; Sun, X.; Dong, W. Lunar Regolith Geopolymer Concrete for In-Situ Construction of Lunar Bases: A Review. *Polymers* **2024**, *16*, 1582. [CrossRef]
11. Lee, S.; van Riessen, A. A Review on Geopolymer Technology for Lunar Base Construction. *Materials* **2022**, *15*, 4516. [CrossRef] [PubMed]
12. Ryu, G.S.; Lee, Y.B.; Koh, K.T.; Chung, Y.S. The Mechanical Properties of Fly Ash-Based Geopolymer Concrete with Alkaline Activators. *Constr. Build. Mater.* **2013**, *47*, 409–418. [CrossRef]
13. Kong, D.L.Y.; Sanjayan, J.G. Effect of Elevated Temperatures on Geopolymer Paste, Mortar and Concrete. *Cem. Concr. Res.* **2010**, *40*, 334–339. [CrossRef]
14. Bernal, S.A.; Mejía de Gutiérrez, R.; Provis, J.L. Engineering and Durability Properties of Concretes Based on Alkali-Activated Granulated Blast Furnace Slag/Metakaolin Blends. *Constr. Build. Mater.* **2012**, *33*, 99–108. [CrossRef]
15. Sbahieh, S.; McKay, G.; Al-Ghamdi, S.G. Comprehensive Analysis of Geopolymer Materials: Properties, Environmental Impacts, and Applications. *Materials* **2023**, *16*, 7363. [CrossRef]
16. Sambucci, M.; Sibai, A.; Valente, M. Recent Advances in Geopolymer Technology. A Potential Eco-Friendly Solution in the Construction Materials Industry: A Review. *J. Compos. Sci.* **2021**, *5*, 109. [CrossRef]
17. Diaz-Loya, I.E.; Allouche, E.N.; Vaidya, S. Mechanical Properties of Fly-Ash-Based Geopolymer Concrete. *ACI Mater. J.* **2011**, *108*, 300–306. [CrossRef]
18. Das, S.; Saha, P.; Prajna Jena, S.; Panda, P. Geopolymer Concrete: Sustainable Green Concrete for Reduced Greenhouse Gas Emission—A Review. *Mater. Today Proc.* **2022**, *60*, 62–71. [CrossRef]
19. Cong, P.; Du, R.; Gao, H.; Chen, Z. Comparison and Assessment of Carbon Dioxide Emissions between Alkali-Activated Materials and OPC Cement Concrete. *J. Traffic Transp. Eng. (Engl. Ed.)* **2024**, *11*, 918–938. [CrossRef]
20. Shao, R.; Wu, C.; Li, J. Innovative Development of Geopolymer-Based Lunar High Strength Concrete for Sustainable Extra-Terrestrial Construction Using Large-Scale Regolith Simulants. *Constr. Build. Mater.* **2024**, *450*, 138707. [CrossRef]
21. Long-Fox, J.M.; Landsman, Z.A.; Easter, P.B.; Millwater, C.A.; Britt, D.T. Geomechanical Properties of Lunar Regolith Simulants LHS-1 and LMS-1. *Adv. Space Res.* **2023**, *71*, 5400–5412. [CrossRef]
22. Taylor, G.J.; Martel, L.M.V.; Lucey, P.G.; Gillis-Davis, J.J.; Blake, D.F.; Sarrazin, P. Modal Analyses of Lunar Soils by Quantitative X-Ray Diffraction Analysis. *Geochim. Cosmochim. Acta* **2019**, *266*, 17–28. [CrossRef]
23. Taylor, L.A.; Liu, Y. Important Considerations for Lunar Soil Simulants. In *Proceedings of the Earth and Space 2010*; American Society of Civil Engineers: Reston, VA, USA, 2010; pp. 106–118.
24. Zarzycki, P.K.; Katzer, J. Multivariate Comparison of Lunar Soil Simulants. *J. Aerosp. Eng.* **2019**, *32*, 06019005. [CrossRef]
25. Sun, Y.; Ma, S.; Chen, Q.; Chen, G.; He, P.; Wang, Y.; Qiu, J.; Jia, D. Lunar Regolith Simulant-Derived 3D-Printed Geopolymers with Optimized Mechanical and Thermal Management Properties. *Compos. Part A Appl. Sci. Manuf.* **2025**, *196*, 108989. [CrossRef]
26. Barve, P.; Bahrami, A.; Shah, S. Geopolymer 3D Printing: A Comprehensive Review on Rheological and Structural Performance Assessment, Printing Process Parameters, and Microstructure. *Front. Mater.* **2023**, *10*, 1241869. [CrossRef]
27. Raj, A.; Sathyan, D.; Mini, K.M. Physical and Functional Characteristics of Foam Concrete: A Review. *Constr. Build. Mater.* **2019**, *221*, 787–799. [CrossRef]
28. Fu, Y.; Wang, X.; Wang, L.; Li, Y. Foam Concrete: A State-of-the-Art and State-of-the-Practice Review. *Adv. Mater. Sci. Eng.* **2020**, *2020*, 6153602. [CrossRef]
29. Bai, C.; Colombo, P. Processing, Properties and Applications of Highly Porous Geopolymers: A Review. *Ceram. Int.* **2018**, *44*, 16103–16118. [CrossRef]
30. Novais, R.M.; Pullar, R.C.; Labrincha, J.A. Geopolymer Foams: An Overview of Recent Advancements. *Prog. Mater. Sci.* **2020**, *109*, 100621. [CrossRef]
31. Jaya, N.A.; Yun-Ming, L.; Cheng-Yong, H.; Abdullah, M.M.A.B.; Hussin, K. Correlation between Pore Structure, Compressive Strength and Thermal Conductivity of Porous Metakaolin Geopolymer. *Constr. Build. Mater.* **2020**, *247*, 118641. [CrossRef]
32. Hajimohammadi, A.; Ngo, T.; Mendis, P. Enhancing the Strength of Pre-Made Foams for Foam Concrete Applications. *Cem. Concr. Compos.* **2018**, *87*, 164–171. [CrossRef]
33. Ducman, V.; Korat, L. Characterization of Geopolymer Fly-Ash Based Foams Obtained with the Addition of Al Powder or $H_2O_2$ as Foaming Agents. *Mater. Charact.* **2016**, *113*, 207–213. [CrossRef]
34. Rizal, F.; Pratama, A.P.; Khamistan; Fauzi, A.; Syarwan; Azka, A. Effect of $H_2O_2$ as the Foaming Agent on the Geopolymer Mortar Using Curing of Room Temperature. *IOP Conf. Ser. Mater. Sci. Eng.* **2020**, *854*, 012022. [CrossRef]

35. Walbrück, K.; Maeting, F.; Witzleben, S.; Stephan, D. Natural Fiber-Stabilized Geopolymer Foams—A Review. *Materials* **2020**, *13*, 3198. [CrossRef]
36. Cho, S.; van Rooyen, A.; Kearsley, E.; van Zijl, G. Foam Stability of 3D Printable Foamed Concrete. *J. Build. Eng.* **2022**, *47*, 103884. [CrossRef]
37. Franchin, G.; Scanferla, P.; Zeffiro, L.; Elsayed, H.; Baliello, A.; Giacomello, G.; Pasetto, M.; Colombo, P. Direct Ink Writing of Geopolymeric Inks. *J. Eur. Ceram. Soc.* **2017**, *37*, 2481–2489. [CrossRef]
38. Gasmi, A.; Pélegris, C.; Davidovits, R.; Guessasma, M.; Tortajada, H.; Jean, F. Advanced Refinement of Geopolymer Composites for Enhanced 3D Printing via In-Depth Rheological Insights. *Ceramics* **2024**, *7*, 1316–1339. [CrossRef]
39. Sikora, P.; Chougan, M.; Cuevas, K.; Liebscher, M.; Mechtcherine, V.; Ghaffar, S.H.; Liard, M.; Lootens, D.; Krivenko, P.; Sanytsky, M.; et al. The Effects of Nano- and Micro-Sized Additives on 3D Printable Cementitious and Alkali-Activated Composites: A Review. *Appl. Nanosci.* **2022**, *12*, 805–823. [CrossRef]
40. Long-Fox, J.M.; Britt, D.T. Characterization of Planetary Regolith Simulants for the Research and Development of Space Resource Technologies. *Front. Space Technol.* **2023**, *4*, 1255535. [CrossRef]
41. Stiernstedt, J.; Fröberg, J.C.; Tiberg, F.; Rutland, M.W. Forces between Silica Surfaces with Adsorbed Cationic Surfactants: Influence of Salt and Added Nonionic Surfactants. *Langmuir* **2005**, *21*, 1875–1883. [CrossRef] [PubMed]
42. Li, P.; Ren, X.; Chen, Y.; Zhang, Z.; Kang, J.; Li, Y. Equilibrium and Dynamic Surface Properties of Cationic/Anionic Surfactant Mixtures Based on Alcohol Ether Sulfate. *J. Dispers. Sci. Technol.* **2024**, *45*, 909–918. [CrossRef]
43. Chalah, K.; Hammiche, D.; Bennnoui, I.; Benmounah, A. Evaluation of Shear Yield Stress and Apparent Viscosity of Xanthan Gum Solutions: Application of Rheological Models and Analytical Study. *Macromol. Res.* **2025**, *33*, 423–437. [CrossRef]
44. Maierdan, Y.; Zhao, D.; Chokshi, P.H.; Garmonina, M.; Kawashima, S. Rheology, 3D Printing, and Particle Interactions of Xanthan Gum-Clay Binder for Earth Concrete. *Cem. Concr. Res.* **2024**, *182*, 107551. [CrossRef]
45. Amankeldi, F.; Ospanova, Z.; Abdushukur, K.; Musabekov, K.; Miller, R. Effect of Bentonite Clay Particles on the Behavior of Foam Stabilized by SDS–PVA Complexes. *Results Surf. Interfaces* **2022**, *8*, 100073. [CrossRef]
46. Zhang, X.; Bai, C.; Qiao, Y.; Wang, X.; Jia, D.; Li, H.; Colombo, P. Porous Geopolymer Composites: A Review. *Compos. Part A Appl. Sci. Manuf.* **2021**, *150*, 106629. [CrossRef]
47. Driouich, A.; Dalconi, M.C.; Franchin, G.; Bettanini, C.; Santini, E.; Gioia, F.; Esposito, C.; Valentini, L. Optimization of Alkali-Activated Regolith Simulants for Lunar Construction by 3D Printing. In *Proceedings of the RILEM Spring Convention and Conference 2025*; Springer: Cham, Switzerland, 2026; pp. 197–207.
48. Llamas, S.; Ponce Torres, A.; Liggieri, L.; Santini, E.; Ravera, F. Surface Properties of Binary $TiO_2$-$SiO_2$ Nanoparticle Dispersions Relevant for Foams Stabilization. *Colloids Surf. A Physicochem. Eng. Asp.* **2019**, *575*, 299–309. [CrossRef]
49. Arriaga, L.R.; Drenckhan, W.; Salonen, A.; Rodrigues, J.A.; Íñiguez-Palomares, R.; Rio, E.; Langevin, D. On the Long-Term Stability of Foams Stabilised by Mixtures of Nano-Particles and Oppositely Charged Short Chain Surfactants. *Soft Matter* **2012**, *8*, 11085. [CrossRef]
50. Xue, Q.; Zhang, L.; Mei, K.; Li, X.; Wang, Y.; Cheng, X.; Fu, X. Thermal Conductivity and Pore Structure Analysis of Alkali-Activated Foam Cement with Supercritical $CO_2$ Modified Slag: Feasibility Evaluation for Geothermal Applications. *Constr. Build. Mater.* **2022**, *347*, 128506. [CrossRef]
51. Rashad, A.M.; Mosleh, Y.A.; Mokhtar, M.M. Thermal Insulation and Durability of Alkali-Activated Lightweight Slag Mortar Modified with Silica Fume and Fly Ash. *Constr. Build. Mater.* **2024**, *411*, 134255. [CrossRef]
52. Lamch, Ł.; Leszczyńska, I.; Długowska, D.; Szczęsna-Górniak, W.; Batys, P.; Jarek, E.; Wilk, K.A.; Warszyński, P. Synthesis of New Cationic Dicephalic Surfactants and Their Nonequivalent Adsorption at the Air/Solution Interface. *Langmuir* **2025**, *41*, 8125–8137. [CrossRef]
53. Zhang, C.; Geng, T.; Jiang, Y.; Zhao, L.; Ju, H.; Wang, Y. Impact of NaCl Concentration on Equilibrium and Dynamic Surface Adsorption of Cationic Surfactants in Aqueous Solution. *J. Mol. Liq.* **2017**, *238*, 423–429. [CrossRef]
54. Peng, M.; Duignan, T.T.; Nguyen, C.V.; Nguyen, A.V. From Surface Tension to Molecular Distribution: Modeling Surfactant Adsorption at the Air–Water Interface. *Langmuir* **2021**, *37*, 2237–2255. [CrossRef] [PubMed]
55. Harikrishnan, A.R.; Dhar, P.; Agnihotri, P.K.; Gedupudi, S.; Das, S.K. Effects of Interplay of Nanoparticles, Surfactants and Base Fluid on the Surface Tension of Nanocolloids. *Eur. Phys. J. E* **2017**, *40*, 53. [CrossRef]
56. Doroudian Rad, M.; Telmadarreie, A.; Xu, L.; Dong, M.; Bryant, S.L. Insight on Methane Foam Stability and Texture via Adsorption of Surfactants on Oppositely Charged Nanoparticles. *Langmuir* **2018**, *34*, 14274–14285. [CrossRef]
57. Shojaei, M.J.; Méheust, Y.; Osman, A.; Grassia, P.; Shokri, N. Combined Effects of Nanoparticles and Surfactants upon Foam Stability. *Chem. Eng. Sci.* **2021**, *238*, 116601. [CrossRef]
58. Gholipour-Sangelaji, K.; Hosseini-Nasab, S.M.; Hormozi, F. Experimental Study on Mechanisms of Hybrid Effects of Different Surfactant Types on Nano-Particle Wettability to Enhance Foam Stability. *ACS Omega* **2025**, *10*, 28836–28847. [CrossRef] [PubMed]

59. Zaafouri, Z.; Bauer, D.; Batôt, G.; Nieto-Draghi, C.; Coasne, B. Cooperative Effects Dominating the Thermodynamics and Kinetics of Surfactant Adsorption in Porous Media: From Lateral Interactions to Surface Aggregation. *J. Phys. Chem. B* **2020**, *124*, 10841–10849. [CrossRef]
60. Chen, Z.; Wang, X.; Giuliani, F.; Atkinson, A. Microstructural Characteristics and Elastic Modulus of Porous Solids. *Acta Mater.* **2015**, *89*, 268–277. [CrossRef]
61. Biswas, P.; Ma, J. Spatial Pore Distribution: An Approach to Uncouple the Strength–Porosity Trade-Offs. *J. Mater. Sci.* **2022**, *57*, 411–421. [CrossRef]
62. Guarino, V.; Causa, F.; Ambrosio, L. Porosity and Mechanical Properties Relationship in PCL Porous Scaffolds. *J. Appl. Biomater. Biomech.* **2007**, *5*, 149–157.